

## Competing Structural Influences in the Li Superionic Conducting Argyrodites $\text{Li}_6\text{PS}_{5-x}\text{Se}_x\text{Br}$ ( $0 \leq x \leq 1$ ) upon Se Substitution

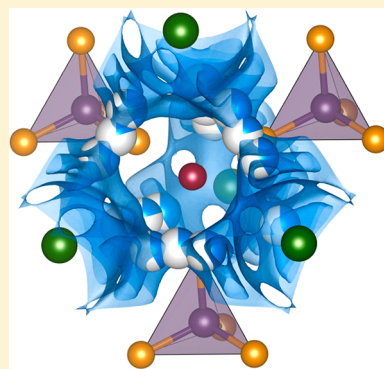
Tim Bernges,<sup>†,‡</sup> Sean P. Culver,<sup>†,‡</sup> Nicolò Minafra,<sup>†,‡</sup> Raimund Koerver,<sup>†,‡</sup> and Wolfgang G. Zeier<sup>\*,†,‡,§</sup>

<sup>†</sup>Institute of Physical Chemistry, Justus-Liebig-University Giessen, Heinrich-Buff-Ring 17, D-35392 Giessen, Germany

<sup>‡</sup>Center for Materials Research (LaMa), Justus-Liebig-University Giessen, Heinrich-Buff-Ring 16, D-35392 Giessen, Germany

### Supporting Information

**ABSTRACT:** Lithium-ion conducting argyrodites have recently attracted significant interest as solid electrolytes for solid-state battery applications. In order to enhance the utility of materials in this class, a deeper understanding of the fundamental structure–property relationships is still required. Using Rietveld refinements of X-ray diffraction data and pair distribution function analysis of neutron diffraction data, coupled with electrochemical impedance spectroscopy and speed of sound measurements, the structure and transport properties within  $\text{Li}_6\text{PS}_{5-x}\text{Se}_x\text{Br}$  ( $0 \leq x \leq 1$ ) have been monitored with increasing Se content. While it has been previously suggested that the incorporation of larger, more polarizable anions within the argyrodite lattice should lead to enhancements in the ionic conductivity, the  $\text{Li}_6\text{PS}_{5-x}\text{Se}_x\text{Br}$  transport behavior was found to be largely unaffected by the incorporation of  $\text{Se}^{2-}$  due to significant structural modifications to the anion sublattice. This work affirms the notion that, when optimizing the ionic conductivity of solid ion conductors, local structural influences cannot be ignored and the idea of “the softer the lattice, the better” does not always hold true.



### 1. INTRODUCTION

Over the past few years, solid ion conductors have garnered considerable attention due to their potential as separators in solid-state lithium-ion-battery applications.<sup>1–3</sup> The employment of solid electrolytes possessing high ionic conductivities, thereby replacing the ubiquitous liquid electrolytes used in conventional lithium-ion batteries, enables the realization of safer and more reliable batteries with higher energy and power densities. Among the myriad of solid electrolytes that are currently available, the class of lithium thiophosphates have been found to exhibit some of the most exceptional ionic conductivities, e.g.,  $\text{Li}_{10}\text{MP}_2\text{S}_{12}$ ,<sup>4–11</sup>  $\text{Li}_7\text{P}_3\text{S}_{11}$ ,<sup>12–14</sup> thiophosphate glass ceramics,<sup>15–19</sup> and the  $\text{Li}_6\text{PS}_5\text{X}$  argyrodites,<sup>20–24</sup> among others.<sup>25</sup> Nevertheless, a better understanding of the principles governing ionic transport in solid ion conductors is still required in order to access the next generation of electrolyte materials.

Figure 1a shows the fully ordered unit cell of the  $\text{Li}_6\text{PCh}_5\text{Br}$  ( $\text{Ch} = \text{chalcogenide}$ ) argyrodite structure. Therein, the corner and face-centered positions of the cubic lattice (Wyckoff 4a) are occupied by the  $\text{Br}^-$  anions. Meanwhile, the  $\text{PCh}_4$  polyhedra reside on the octahedral sites (with P on Wyckoff 4b) and the tetrahedral voids are partially occupied by the free chalcogenide anions (Wyckoff 4d). Importantly, a high degree of site disorder between  $\text{Br}^-$  and  $\text{Ch}^{2-}$  in  $\text{Li}_6\text{PS}_5\text{Br}$  is known to exist and has been shown to influence the ionic conductivity.<sup>20,26</sup> As shown in Figure 1b, the chemical identity of the anion framework surrounding the mobile lithium ions significantly influences the associated diffusion. The available

sites for the lithium ions (Wyckoff 48h and 24g) form cage-like polyhedra around the free chalcogenide anions, enabling three different jump processes to occur during ionic transport: lithium ion jumps between neighboring lithium positions (48h–24g–48h; doublet jump), intracage jumps (48h–48h), and intercage jumps (48h–48h), as shown in Figure 1b.

In this work, the substitution of  $\text{S}^{2-}$  by  $\text{Se}^{2-}$  was performed within  $\text{Li}_6\text{PS}_{5-x}\text{Se}_x\text{Br}$  ( $0 \leq x \leq 1$ ) in order to assess the influence of incorporating a larger, more polarizable anion upon the free sulfur site 4d on the resultant structure and lithium transport behavior, while maintaining the existing diffusion pathways. The goal of this study is twofold: (1) The incorporation of larger and less electronegative atoms has been predicted to enhance the ionic conductivity.<sup>24</sup> In theory, incorporating larger, more polarizable anions in the argyrodite lattice should broaden the lithium diffusion pathways and weaken interactions between  $\text{Li}^+$  and the anion framework due to changing lattice dynamics, leading to an increase in the associated ionic conductivity. (2) In addition, by substituting only the free chalcogen site, it may be possible to alter the known site disorder between  $\text{Br}^-$  and  $\text{Ch}^{2-}$ .

Using a combination of X-ray diffraction, neutron pair distribution function, impedance spectroscopy, and ultrasonic sound response measurements, this work shows that, in the  $\text{Li}_6\text{PS}_{5-x}\text{Se}_x\text{Br}$  system, the potential for structural changes that alter the interactions between the mobile  $\text{Li}^+$  atoms and the

Received: August 29, 2018

Published: October 22, 2018

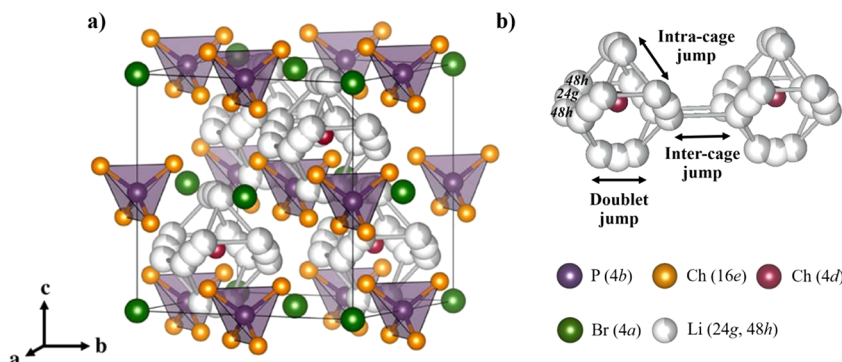


**Figure 1.** (a) Ordered crystal structure of  $\text{Li}_6\text{PCh}_5\text{Br}$ . The  $\text{Br}^-$  anions form a cubic close packed lattice with  $\text{PCh}_4$  tetrahedra in the octahedral sites and the free  $\text{Ch}^{2+}$  in half of the tetrahedral sites (Wyckoff 4d). (b) The Li positions form localized cages in which multiple jump processes are possible. Jumps between the lithium positions ( $48h-24g-48h$ ; doublet jump), intracage jumps ( $48h-48h$ ), and intercage jumps ( $48h-48h$ ) can occur.

anion framework complicates this conductivity enhancement strategy. While the larger anion broadens the lithium diffusion pathways, a local structural reordering and loss of site disorder counters the beneficial, wider diffusion pathways. In addition, the changing lattice dynamics affect the activation energy and prefactor, as they are decreased for the compounds with a softer lattice. This work shows the importance of local structural considerations in the development of ionic conductivity enhancement strategies and that “the softer the lattice, the better” does not always apply.

## 2. EXPERIMENTAL METHODS

**Synthesis.** All preparations and sample treatments were carried out under an Ar atmosphere. Lithium sulfide ( $\text{Li}_2\text{S}$ , Sigma-Aldrich, 99.98%), lithium bromide ( $\text{LiBr}$ , ChemPur, 99.995%), P (ChemPur, 99.999%), S (Acros Organics, 99.999%), and Se (Alfa Aesar, 99.99%) were mixed in the appropriate stoichiometric ratios using an agate mortar. The precursor mixtures were pressed into pellets and sealed in quartz ampoules (10 mm inner diameter and 10–12 cm in length) under vacuum. All ampoules were carbon-coated and preheated at 800 °C under dynamic vacuum for 3 h to avoid all traces of water in the reaction atmosphere. The reaction mixtures were treated at 550 °C for 2 weeks to ensure reaction completeness and the phase purity of the products.

**X-ray Powder Diffraction.** Powder X-ray diffraction measurements were carried out using an Empyrean diffractometer (PANalytical, Netherlands) with  $\text{Cu K}\alpha$  radiation ( $\lambda_1 = 1.54051 \text{ \AA}$ ,  $\lambda_2 = 1.54433 \text{ \AA}$ ) in Bragg–Brentano  $\theta-\theta$  geometry using a PIXcel3D area detector with 255 measuring channels. Samples were pulverized and placed on (911)-oriented silicon zero diffraction holders and sealed with Kapton foil. Measurements have been performed within a  $2\theta$  range of 10–90° with a step size of 0.026° and 180 s per step.

**Rietveld Analysis.** Rietveld refinements were carried out using the TOPAS software package.<sup>27</sup> The peak profile shape was described by a pseudo-Voigt function using the modified Thomson–Cox–Hastings setting. Fit indicators:  $R_{wp}$ ,  $R_{exp}$ , and GoF were used to assess the quality of the refined structural models. The following parameters were initially refined: (1) scale factor, (2) background coefficients, (3) peak shape, (4) lattice constants, (5) fractional atomic coordinates of the sulfur atoms on the Wyckoff 16e site, (6) isotropic atomic displacement parameters, and (7) sample displacement. The Se content was fixed to the nominal value for all refinements, given the strong agreement with the experimental stoichiometry determined by energy dispersive X-ray spectroscopy (Figure S1 and Table S1). In addition, as X-rays are not able to resolve the lithium occupancies, these values were fixed on the basis of previously obtained structural data extracted from neutron diffraction data of  $\text{Li}_6\text{PS}_5\text{Br}$ .<sup>20</sup> The atomic occupancies of S and Se on the Wyckoff 16e position were refined in order to quantify the exchange between S and Se on the

Wyckoff 4a and 16e positions. Finally, atomic occupancies of Br and S were refined in order to quantify the anion site disorder in  $\text{Li}_6\text{PS}_{5-x}\text{Se}_x\text{Br}$  ( $x = 0, 0.1$ , and  $0.2$ ) between Br (Wyckoff 4a) and S (Wyckoff 4d). Beyond this range of Se incorporation, the similar electron densities of Se and Br inhibited the deconvolution of the  $\text{Br}^-/\text{S}^{2-}$  exchange on the Wyckoff 4d and 4a sites, respectively.

**Neutron Pair Distribution Function Analysis.** Quartz capillaries with an outer diameter of 0.9 mm were filled in an argon glovebox and sealed using epoxy. Neutron scattering data suitable for pair distribution function analysis were collected at room temperature using the TOF NOMAD instrument at the Oak Ridge National Laboratory beamline (Oak Ridge, TN).

The crystallographic data, obtained from the refinements of the Bragg data, were used as starting values for the analysis of the PDF data of  $\text{Li}_6\text{PS}_{5-x}\text{Se}_x\text{Br}$  ( $x = 0, 0.5, 1.0$ ). The pair distribution function  $G(r)$  was employed for a more accurate structural analysis, and the Oak Ridge software was used to extract  $G(r)$  from the raw diffraction data. A maximum scattering vector ( $Q_{\max}$ ) of  $22 \text{ \AA}^{-1}$  was employed in the Fourier transform. Structural refinements were carried out using the PDFgui software.<sup>28</sup> The local crystal structure of the  $\text{Li}_6\text{PS}_{5-x}\text{Se}_x\text{Br}$  crystallites was refined with the  $F\bar{4}3m$  space group. The fit of this structural model to the experimental PDF data was performed in the 1.8–30 Å interatomic distance range. The following parameters were refined: (1) scale factor, (2) lattice constants, (3) local correlated motion factor, (4) fractional atomic coordinates of the lithium atoms and the sulfur atoms on the Wyckoff 16e site, and (5) atomic isotropic displacement parameters. The Se content was fixed to the nominal content for all refinements, given the strong agreement with the experimental stoichiometry determined by energy dispersive X-ray spectroscopy (Figure S1 and Table S1). The atomic occupancies of S and Se on the Wyckoff 16e position were refined in order to quantify the exchange between S and Se on the Wyckoff 4a and 16e positions. Finally, atomic occupancies of Br, S, and Se were refined in order to quantify the anion site disorder between Br (Wyckoff 4a) and S/Se (Wyckoff 4d). The  $R_w$  indicator was employed to assess the quality of the refined structural models.

**Electrochemical Impedance Spectroscopy.** Electrical conductivities were measured by AC impedance spectroscopy, using isostatically pressed pellets (325 MPa, 3.0 mm thickness, 9.5 mm diameter, geometric density of all samples >83%) that have been rapidly annealed at 550 °C for 10 min in an evacuated quartz ampule and were afterward gold coated with thin gold (200 nm) electrodes. Electrochemical impedance analysis was conducted in the temperature range 233–333 K using an SP300 impedance analyzer (Biologic) at frequencies from 7 MHz to 100 mHz with an amplitude of 10 mV.

**Ultrasonic Speed of Sound Measurements.** Pulse-echo speed of sound measurements were performed on consolidated discs using an Epoch 600 (Olympus) with 5 MHz transducers for longitudinal and transverse speeds of sound. The samples were coated with a thin

layer (<200 nm) of gold in order to prevent side reactions of the couplant and the sample. All measurements were performed under a nitrogen atmosphere. The measurement uncertainty from the speed of sound data results stems from the uncertainty in the thickness and the porosity. As the measurement uncertainty for the thickness of the pellet is much higher than that of the gold layer, the thin layer of Au is not expected to add significantly to the measurement uncertainty. In addition, no damping of the signal is expected due to the high crystallinity and high speed of sound in Au. This measurement procedure has recently been shown to be successful in understanding the lattice softness of thiophosphates.<sup>20,29–31</sup>

The obtained longitudinal and transverse speeds of sound  $v_{\text{long}}$  and  $v_{\text{trans}}$  can be used to calculate the mean speed of sound  $v_{\text{mean}}$  as well as the Debye frequency  $\nu_D$  via eqs 1 and 2.<sup>32,33</sup>

$$v_{\text{mean}} = \frac{3}{v_{\text{long}}^{-3} + 2v_{\text{trans}}^{-3}} \quad (1)$$

$$\nu_D = \left( \frac{3}{4\pi V} \right)^{1/3} \cdot v_{\text{mean}} \quad (2)$$

### 3. RESULTS

**Structural Characterization.** The Li<sup>+</sup> superionic argyrodites Li<sub>6</sub>PS<sub>5-x</sub>Se<sub>x</sub>Br ( $0 \leq x \leq 1$ ) have been synthesized in order to study the influence of (1) increasing the anion polarizability and (2) replacing the free S<sup>2-</sup> site with Se<sup>2-</sup> on both the structure and the transport properties. In the case of (1), the replacement of sulfur with the larger and more polarizable selenium is expected to affect the lattice dynamics and expand the unit cell volume, both of which should in turn affect the ionic transport.<sup>24,31,34</sup> In the case of (2), site disorder between the free S<sup>2-</sup> (Wyckoff 4d) and Br<sup>-</sup> (Wyckoff 4a) has been shown to affect the activation barrier for ionic motion,<sup>20</sup> as it controls the bottleneck of the intercage jumps, in which more site disorder seems to be beneficial for the long-range transport. In addition, it was recently shown that the X<sup>-</sup>/S<sup>2-</sup> site disorder decreases when the size mismatch between the sulfur and the halide anions increases.<sup>20</sup>

To take a closer look at the structural influences of Se incorporation on the resultant argyrodite structure, Rietveld refinements of powder X-ray diffraction patterns were performed. Additionally, due to the low X-ray form factor of Li<sup>+</sup>, as well as the nearly identical electron densities of Br<sup>-</sup> and Se<sup>2-</sup>, and with it their scattering form factor for X-rays, selected samples ( $x = 0, 0.5, 1.0$ ) were also investigated using neutron pair distribution function (PDF) analysis. Employment of a neutron PDF analysis affords more accurate structural information concerning both the changing Li<sup>+</sup> substructure and the Br<sup>-</sup>/Ch<sup>2-</sup> site disorder.

Figure 2 shows an exemplary Rietveld refinement of the X-ray diffraction data and the PDF analysis of neutron diffraction data for Li<sub>6</sub>PS<sub>4.5</sub>Se<sub>0.5</sub>Br. As can be seen from a visual inspection of the fits and the corresponding quality-of-fit parameters, the herein studied samples are well described by the cubic F43m argyrodite structure. It should be noted that all compounds exhibit minor impurity phase fractions of LiBr and Li<sub>3</sub>OB<sub>3</sub> (<5 wt %), independent of Se content. Nevertheless, the impurities are unlikely to affect the ionic transport or the obtained structural data,<sup>20,21</sup> which can be found tabulated in the Supporting Information (Tables S2–S15).

The relevant structural data extracted from refinements against the X-ray diffraction data and neutron PDF are provided in Figure 3. The lattice parameters, and thus the unit cell volumes, increase linearly with increasing Se content,

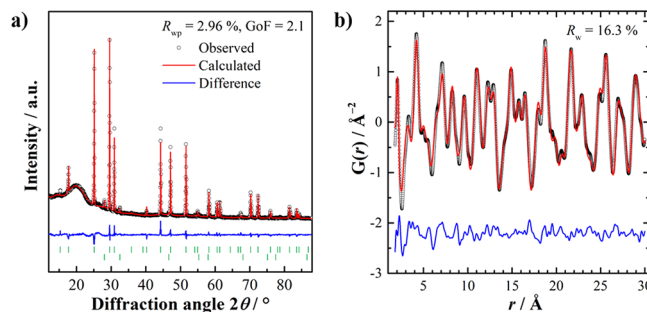


**Figure 2.** (a) X-ray powder diffraction data for Li<sub>6</sub>PS<sub>4.5</sub>Se<sub>0.5</sub>Br and the corresponding Rietveld refinement. A small fraction of a LiBr impurity phase can be seen and was refined to be 2.1 wt %. The measurement using Kapton foil leads to the increased background between 15 and 24°. (b) Neutron pair distribution function  $G(r)$  for Li<sub>6</sub>PS<sub>4.5</sub>Se<sub>0.5</sub>Br and the corresponding structural refinement.

thereby obeying Vegard's law and confirming the successful synthesis of solid solutions within the Li<sub>6</sub>PS<sub>5-x</sub>Se<sub>x</sub>Br ( $0 \leq x \leq 1$ ) series. The observed lattice expansion is induced by the larger ionic radius of Se<sup>2-</sup> (1.98 Å) relative to S<sup>2-</sup> (1.84 Å).<sup>35</sup> Within the argyrodite structure, the chalcogenide anions either coordinate with P<sup>5+</sup> to form PCh<sub>4</sub><sup>3-</sup> tetrahedra or occupy the free Ch<sup>2-</sup> sites (Wyckoff 16e or 4d, respectively). Interestingly, with increasing  $x$ , beyond the increase in the occupancy of the Wyckoff 4d site (i.e., the free Ch<sup>2-</sup> site), an increase in the occupancy of the Wyckoff 16e site by Se can also be seen (Figure 3b). This increasing occupancy of Se on the tetrahedra drives the observed expansion of the PCh<sub>4</sub> tetrahedra (Figure 3c). At the composition of Li<sub>6</sub>PS<sub>4</sub>SeBr, approximately 50% of the selenium occupy the free Ch<sup>2-</sup> site, with the other half replacing sulfur on the PS<sub>4</sub><sup>3-</sup> tetrahedra. The increasing occupancy of the 16e site by Se was further corroborated by Raman spectroscopy (Figure S2). Here, as the occupancy of the 16e site by Se increases, the formation of PS<sub>3</sub>Se<sup>3-</sup> tetrahedra breaks the tetrahedral symmetry of the PCh<sub>4</sub> units and augments the intensity of the symmetric stretching mode at 367 cm<sup>-1</sup> with increasing  $x$ .

As described above, site disorder between Br<sup>-</sup> and the chalcogenide anions is also known to occur,<sup>20,22,26</sup> in which the free chalcogenide anions exchange with Br<sup>-</sup> to additionally occupy the Wyckoff 4a sites. Figure 3d shows the obtained disorder between Br<sup>-</sup> and Ch<sup>2-</sup>, and the percentage of disorder shown represents the total fraction of Br<sup>-</sup> on the Ch<sup>2-</sup> site. Given the similar X-ray scattering form factors of Br<sup>-</sup> and Se<sup>2-</sup>, only exchange between Br<sup>-</sup> and S<sup>2-</sup> was refined from the X-ray scattering data for  $x = 0, 0.1$ , and 0.2. Beyond this compositional range, the refinement of the site disorder was unstable due to the increasing Se content and the difficulty in distinguishing Br<sup>-</sup> and Se<sup>2-</sup>. Fortunately, Br and Se are distinguishable by neutron diffraction, and thus, both types of exchange (i.e., S<sup>2-</sup> and Se<sup>2-</sup>) with Br<sup>-</sup> could be adequately refined for  $x = 0, 0.5$ , and 1.0 using the neutron pair distribution function data. There are no unexpected variations in the local structure, as seen in the  $G(r)$ , and a good agreement can be found between the refined X-ray and neutron diffraction data, where the obtained disorder for Li<sub>6</sub>PS<sub>5</sub>Br was approximately 23% and rapidly decreases with increasing Se content. While the refined site disorder in Li<sub>6</sub>PS<sub>5</sub>Br confirms the values found by Kraft et al.<sup>20</sup> and Minafra et al.,<sup>21</sup> the decreasing disorder remains puzzling. Theoretically predicted<sup>26</sup> and experimentally confirmed,<sup>20</sup> a

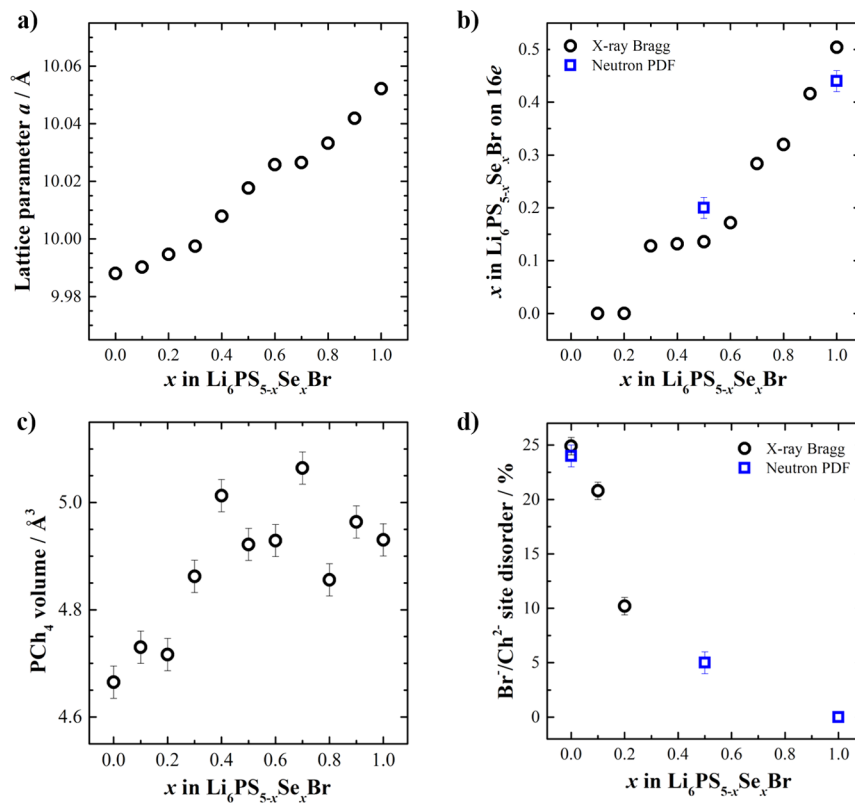


**Figure 3.** Structural data of  $\text{Li}_6\text{PS}_{5-x}\text{Se}_x\text{Br}$  obtained from Rietveld refinements of X-ray diffraction data and the PDF analysis of neutron diffraction data. (a) Increasing lattice parameters arising from the incorporation of larger  $\text{Se}^{2-}$  atoms. (b) Increasing  $\text{Se}^{2-}$  occupancy on the 16e Wyckoff ( $\text{Ch}^{2-}$  on  $\text{PCh}_4$  tetrahedra) site with increasing  $x$ . (c) Increasing  $\text{PCh}_4$  polyhedral volumes with increasing  $x$ . (d) Decreasing  $\text{Br}^-/\text{Ch}^{2-}$  site disorder with increasing  $x$ . The site disorder in the X-ray data could only be refined between  $x = 0$  and  $x = 0.2$  due to the nearly identical X-ray scattering form factors of  $\text{Br}^-$  and  $\text{Se}^{2-}$ . Errors not shown are smaller than the symbol.

larger anion size mismatch between the halide  $X^-$  and  $\text{S}^{2-}$  leads to a decreasing site disorder in  $\text{Li}_6\text{PS}_5\text{X}$  ( $\text{X} = \text{Cl}, \text{Br}, \text{I}$ ). In the here presented case of replacing  $\text{S}^{2-}$  with  $\text{Se}^{2-}$ , however, the opposite is true. With decreasing size mismatch ( $r(\text{Se}^{2-}) = 1.98 \text{ \AA}$ ,  $r(\text{S}^{2-}) = 1.84 \text{ \AA}$ , and  $r(\text{Br}^-) = 1.96 \text{ \AA}$ ), the site disorder decreases.<sup>35</sup> While the underlying reason for the opposite trend in the evolution of the site disorder remains unknown, it may be related to the substitution of  $\text{S}^{2-}$  by  $\text{Se}^{2-}$  on the 16e position and, with it, the formation of local  $\text{PS}_3\text{Se}_3^{2-}$  tetrahedra. Considering Figure 4d, local changes in the tetrahedra may strongly affect the local ordering of the anions. Furthermore, the absence of site disorder coupled with the small size mismatch between  $\text{S}^{2-}$ ,  $\text{Se}^{2-}$ , and  $\text{Br}^-$  suggests that more subtle electronic structure effects may also be influencing the site disorder. Nevertheless, as site disorder is known to influence the ionic transport, i.e., hindering the intercage jumps at low levels of disorder or in the absence of disorder,<sup>20,26</sup> an influence on the  $\text{Li}^+$  distribution and ionic transport in the herein studied solid solutions can be expected.

Figure 4 shows the effect of Se substitution on the  $\text{Li}^+$  sublattice in  $\text{Li}_6\text{PS}_{5-x}\text{Se}_x\text{Br}$  ( $x = 0, 0.5, 1.0$ ), as obtained from the PDF analysis of the neutron diffraction data. With increasing Se content, the lithium occupancy on the 48h Wyckoff site can be seen to increase, with a concurrent decrease in the occupancy of the 24g transition state (Figure 4a). Considering the coordination of  $\text{Li}^+$  (48h) around the free  $\text{Ch}^{2-}$  site, forming clusters of lithium (Figure 1b), one may expect that the reduced site disorder, and with it the higher charge density of  $\text{Ch}^{2-}$  vs  $\text{Br}^-$ , leads to a higher occupancy of

$\text{Li}^+$  on the 48h site. The higher occupancy on the 48h site leads to more Coulombic repulsion between these two sites, which concurrently increases the doublet jump distance 48h–24g–48h and decreases the intercage jump (see Figure 4b). While the occupancies of the different positions change, there seems to be no significant change in the Li positions to suggest altered diffusion trajectories, in accordance with the work by Kraft et al.<sup>20</sup> In addition to the  $\text{Li}^+$  occupancies and jump distances, the width of the diffusion pathway is important in ionic conductors.<sup>30,36</sup> The Li ions on the Wyckoff 48h position are coordinated by three  $\text{Ch}^{2-}$  and one  $\text{Br}^-$ , forming  $\text{LiCh}_3\text{Br}$  tetrahedra. Meanwhile, the Li ions on the Wyckoff 24g position are coordinated by three sulfur, forming a trigonal planar  $\text{LiS}_3$  arrangement, and correspond to the transition state between the doublet jumps.<sup>20</sup> Depictions of the polyhedra and planes along the conduction pathway, in addition to the variation in the polyhedral volumes and planar areas with changing composition, are provided in Figure 4c and d. With increasing Se content, the unit cell increases and the lithium diffusion pathways also broaden.

**Ionic Transport.** Temperature-dependent electrochemical impedance spectroscopy was performed on all samples to monitor the changes in the ionic conductivity in  $\text{Li}_6\text{PS}_{5-x}\text{Se}_x\text{Br}$  with respect to the Se content. For clarity, only representative Arrhenius plots ( $x = 0, 0.5, 1.0$ ) and a fitted impedance response for  $\text{Li}_6\text{PS}_{4.5}\text{Se}_{0.5}\text{Br}$  are provided in Figure 5a and b, respectively. At lower temperatures, the impedance data were fitted with an equivalent circuit consisting of two parallel CPE/resistors in series with a CPE, representing blocking electrodes

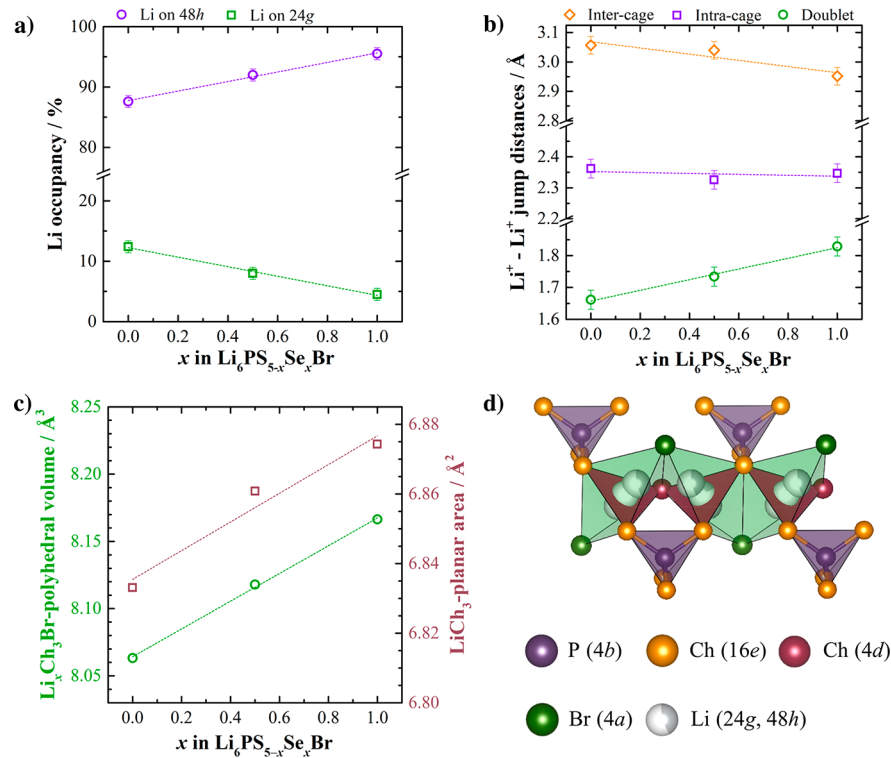


**Figure 4.** Structural data on the  $\text{Li}^+$  sublattice, extracted from the PDF analysis of neutron diffraction data. (a)  $\text{Li}^+$  occupancy on the two available sites, in which the increasing  $\text{Se}^{2-}$  content leads to a decrease in the 24g occupancy. (b)  $\text{Li}^+$ - $\text{Li}^+$  jump distances, which show a decrease in the intercage jump distances with increasing Se content. (c)  $\text{Li}_x\text{Ch}_3\text{Br}$  polyhedral volumes and  $\text{LiCh}_3$  planar areas showing a broadening of the bottleneck. (d) The free  $\text{Ch}^{2-}$  and  $\text{Br}^-$  anions, as well as the corner of the  $\text{PCh}_4$  tetrahedra, enclose two different Li positions (Wyckoff 48h and 24g).

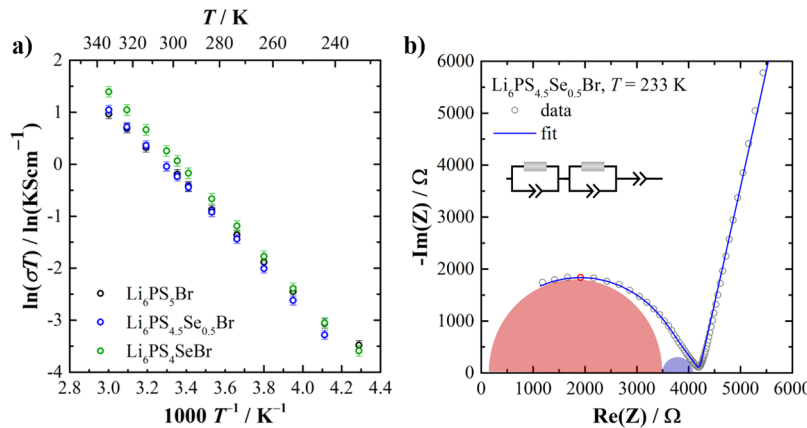


**Figure 5.** (a) Representative Arrhenius plots of the conductivity values for  $\text{Li}_6\text{PS}_{5-x}\text{Se}_x\text{Br}$  ( $x = 0, 0.5, 1.0$ ) obtained from temperature-dependent impedance spectroscopy. (b) Nyquist plot of  $\text{Li}_6\text{PS}_{4.5}\text{Se}_{0.5}\text{Br}$  at 233 K, showing the impedance response and the fit with the provided equivalent circuit. The red semicircle corresponds to the bulk contribution, and the blue semicircle corresponds to the grain-boundary contribution. The apex frequency corresponds to  $1.5 \times 10^6$  Hz (red data point).

(Figure 5b, inset). At temperatures  $>263$  K, the ionic conductivity and relaxation times are so fast and shifted to higher frequencies that they cannot be resolved within the frequency range of the employed impedance analyzer. Conductivity values are then extracted from only fitting the CPE of the blocking electrodes. In the representative impedance response of  $\text{Li}_6\text{PS}_{4.5}\text{Se}_{0.5}\text{Br}$ , two contributions can be found. For the semicircle at high frequencies, an apex frequency of  $1.5 \times 10^6$  Hz and a capacitance of  $7.7 \times 10^{-12}$  F·cm<sup>-2</sup> is obtained. Meanwhile, the second semicircle at midfrequencies exhibits a capacitance of  $2.5 \times 10^{-9}$  F·cm<sup>-2</sup>.

The magnitudes of the capacitances<sup>37</sup> and the ideality of the CPE of the fitted semicircles ( $\alpha = 0.99$ )<sup>38</sup> correspond well with the bulk process at high frequencies and a grain boundary contribution in the midfrequency range. As both processes cannot be resolved at elevated temperatures, the overall ionic conductivities are based on the total conductivity of the samples. However, at 233 K, the grain boundary resistance corresponds to  $\sim 10\%$  of the overall resistance and is clearly decreasing at room temperature. This suggests that the total conductivities can be related to the bulk transport with an upper limit to the uncertainty of  $\sim 10\%$ .

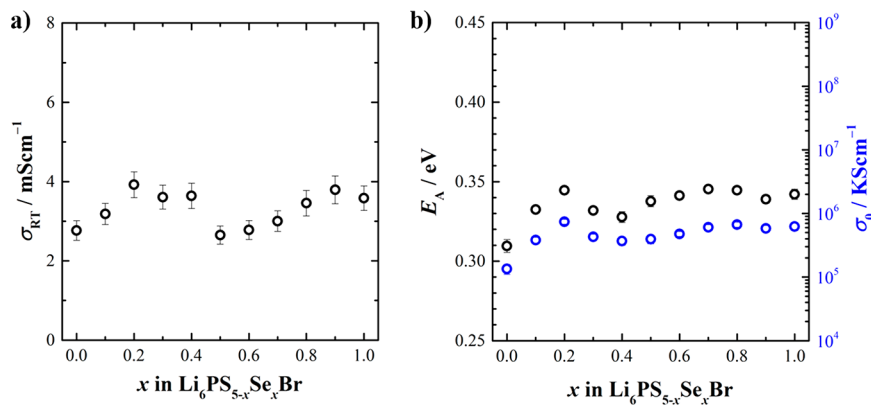


**Figure 6.** (a) Room-temperature conductivity and (b) activation energy  $E_A$  and Arrhenius prefactor  $\sigma_0$  for  $\text{Li}_6\text{PS}_{5-x}\text{Se}_x\text{Br}$  as a function of the Se content. Errors not shown are smaller than the symbol.

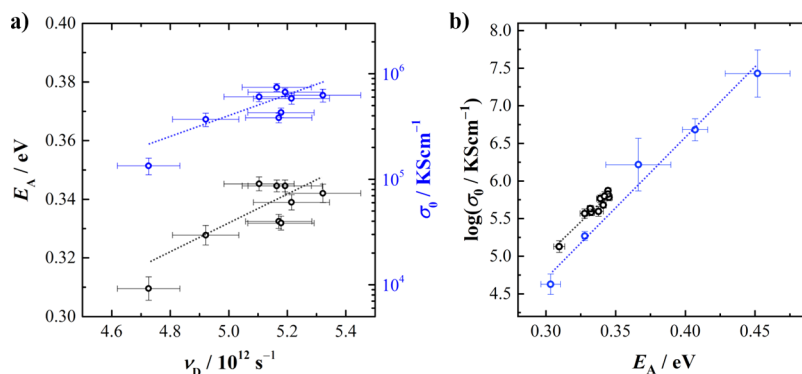


**Figure 7.** (a) Activation energy  $E_A$  and prefactor  $\sigma_0$  as a function of Debye frequency  $\nu_D$  for  $\text{Li}_6\text{PS}_{5-x}\text{Se}_x\text{Br}$ . Both  $E_A$  and  $\sigma_0$  are the lowest when the lattice is soft, as expressed by the decreasing Debye frequency. (b) Meyer–Neldel plot showing the Arrhenius prefactor as a function of activation energy for  $\text{Li}_6\text{PS}_5\text{Cl}_{1-x}\text{Br}_x$  (blue)<sup>20</sup> and  $\text{Li}_6\text{PS}_{5-x}\text{Se}_x\text{Br}$  (black). The dashed lines represent guides to the eye.

Room-temperature ionic conductivities for  $\text{Li}_6\text{PS}_{5-x}\text{Se}_x\text{Br}$  as a function of  $x$  are shown in Figure 6a. The ionic conductivities span from 2.7 to 3.9  $\text{mS}\cdot\text{cm}^{-1}$  over the entire compositional range, showing the fast-ionic conducting nature of the argyrodites. In addition to the room temperature values, the activation barriers  $E_A$  for lithium migration and the Arrhenius prefactors  $\sigma_0$  are shown in Figure 6b. Despite the incorporation of the larger, more polarizable Se anions and the concurrent unit cell expansion, no significant decrease in the activation barrier is observed. While there is no obvious trend in the conductivity with respect to the selenium content, similar to  $\text{Na}_3\text{PS}_{4-x}\text{Se}_x$ ,<sup>31,39,40</sup> the value of 3.9  $\text{mS}\cdot\text{cm}^{-1}$  is the highest reported value for  $\text{Li}^+$  conductivity in the argyrodite structure so far.

#### 4. DISCUSSION

Upon moving from  $\text{Li}_6\text{PS}_5\text{Br}$  to  $\text{Li}_6\text{PS}_4\text{SeBr}$ , a variety of structural changes have been observed that can be used to explain the starting hypothesis that (1) increasing anion polarizability and (2) replacing the free  $\text{S}^{2-}$  site with  $\text{Se}^{2-}$  will affect the structure and ionic transport.

**4.1. Influence of Lattice Softness.** The influence of more polarizable anions on the ionic transport in solids has recently been experimentally corroborated in  $\text{Li}_6\text{PS}_5\text{X}$  ( $\text{X} = \text{Cl}, \text{Br}, \text{I}$ )<sup>20</sup> for  $\text{Li}^+$  transport and  $\text{Na}_3\text{PS}_{4-x}\text{Se}_x$  for  $\text{Na}^+$  transport.<sup>31,41</sup> Using the Debye frequencies obtained from speed of sound measurements, it was found that, with increasing polarizability of the anions, the lattice softness increases. With this increasing

softness of the lattice vibrations, the activation energy  $E_A$  and Arrhenius prefactor  $\sigma_0$  decrease, showing that the paradigm of “the softer, the better” is not entirely correct.<sup>42</sup> On the one hand, the softer vibrational properties of the anion sublattice lead to lower activation barriers, as the oscillatory frequency  $\nu_0$  (or attempt frequency) of the moving ion is related to the activation barrier via:<sup>43</sup>

$$\nu_0 = \frac{1}{a_0} \sqrt{\frac{2E_A}{M_{\text{Li}}}} \quad (3)$$

This attempt frequency is typically approximated by the Debye frequency,<sup>26</sup> and explains the decreasing activation barriers with increasing softness of lattice vibrations.<sup>42</sup> On the other hand, as the entropy of migration<sup>44</sup>  $\Delta S_m$  and the attempt frequency of the moving ion<sup>43</sup> are decreasing with softer lattice vibrations, it directly affects the Arrhenius prefactor  $\sigma_0$ <sup>44</sup>

$$\sigma_0 = \frac{zn(Ze)^2}{k_B} \cdot e^{\Delta S_m/k_B} a_0^2 \nu_0 \quad (4)$$

$$\Delta S_m = k_B \ln \left( \frac{\prod_{i=1}^{3N-1} \nu_i^I}{\prod_{i=1}^{3N-1} \nu_i^S} \right) \quad (5)$$

with a geometrical factor  $z$ , the carrier concentration of mobile ions  $n$ , the jump distance  $a_0$ , and the charge of the ions  $Ze$ . Here, for a small vibration approximation, the entropy of migration is governed by the normal frequencies  $\nu_1, \dots, \nu_N$  for vibrations about the initial and saddle point, I and S,

respectively.<sup>44</sup> Therefore, both the activation barrier and the prefactor are expected to decrease with softer lattices, affecting the overall ionic conductivity  $\sigma$ :

$$\sigma = \frac{\sigma_0}{T} e^{-E_A/(k_B T)} \quad (6)$$

As shown in Figure 7a, in this work, a similar trend of decreasing prefactor and decreasing activation energy with the softening of the lattice (decreasing Debye frequency) can be seen, further corroborating the influence of a softer lattice on ionic transport. The empirical relationship between decreasing  $E_A$  and  $\sigma_0$ , the so-called Meyer–Neldel rule,<sup>45</sup> can be found in Figure 7b. With decreasing activation barrier, the prefactor decreases and does not lead to a tremendous improvement of the overall ionic conductivity. Indeed, the slope of the Meyer–Neldel plot has been linked to the phononic properties of the lattice,<sup>42,46–48</sup> as the overall lattice vibrational properties govern the prefactor and activation barrier and similar slopes are obtained relative to  $\text{Li}_6\text{PS}_5\text{X}$ .<sup>20</sup> Notably, the overall changes in the lattice vibrational frequencies are smaller when compared to  $\text{Li}_6\text{PS}_5\text{X}$  ( $\text{X} = \text{Cl}, \text{Br}, \text{I}$ ) or  $\text{Na}_3\text{PS}_{4-x}\text{Se}_x$ , and  $\text{Li}_6\text{PS}_4\text{SeBr}$  exhibits a stiffer lattice than  $\text{Li}_6\text{PS}_4\text{SBr}$ . This likely stems from the fact that the difference in the electronegativity of the halides is larger, as well as the fact that much lower fractions of S are exchanged for Se (a maximum of 25%) with respect to the whole chalcogenide content. Overall, these data confirm the recently found work on the influence of lattice dynamics on ionic transport; a softer lattice not only affects the enthalpy of migration,<sup>49</sup> and with it the activation barrier, but also affects the prefactor of ionic motion due to the changing entropy of migration and attempt frequencies.<sup>20,31,41,42,46</sup> This shows that further efforts are necessary to break the *prefactor dilemma*<sup>42</sup> arising from the Meyer–Neldel law and that theoretical considerations need to take the lattice dynamics into account.

**4.2. Site Disorder and Diffusion Pathways.** In addition to the concurrent decrease of the prefactor and activation barrier due to the lattice dynamics, the static structural changes play a large role on the ionic conductivity and potential energy landscape.<sup>42</sup> Figure 4 shows that, with increasing unit cell volume due to the larger radius of  $\text{Se}^{2-}$ , the diffusion pathway, as expressed by the  $\text{LiCh}_3\text{Br}$  tetrahedra volumes and  $\text{LiS}_3$  planar areas, increases. While the  $\text{LiS}_3$  planar area only corresponds to the local doublet jump from  $48h$ – $48h$ , the widening of the diffusion pathways with the  $\text{LiCh}_3\text{Br}$  tetrahedra would usually suggest a better ionic conductivity and lower activation barriers for ionic motion.<sup>50</sup> This is a common theme in most ionic conductors, such as the garnets or NASICONs,<sup>36,51,52</sup> in which broader pathways are usually beneficial. However, it has recently been shown that, while in general this assumption is true, local structural changes may interfere.<sup>30</sup> Indeed, especially in the argyrodite structure, the local site disorder between  $\text{X}^-$  and  $\text{Ch}^{2-}$  has been shown to influence the transport,<sup>20,22,26</sup> in which less disorder leads to an increasing activation barrier. In the here studied solid solution  $\text{Li}_6\text{PS}_{5-x}\text{Se}_x\text{Br}$  ( $0 \leq x \leq 1$ ), the  $\text{Br}^-/\text{Ch}^{2-}$  site disorder decreases (as evidenced by the neutron pair distribution function analysis) and vanishes entirely for  $x = 1$ , which should lead to an increase in the activation barrier.<sup>20</sup> It may indeed be the case that site disorder is important when there is a large mismatch between the anion radii such as  $\text{I}^-$  and  $\text{S}^{2-}$ , as seen in the  $\text{Li}_6\text{PS}_5\text{I}$ .<sup>20</sup> At low site disorder, one may expect a narrower bottleneck for the intercage jump, whereas this

disorder effect becomes smaller when the anion-radius mismatch is small, as seen here with  $\text{Br}^-/\text{Ch}^{2-}$  ( $\text{Ch} = \text{S}, \text{Se}$ ).

These data suggest that competing effects are at play in  $\text{Li}_6\text{PS}_{5-x}\text{Se}_x\text{Br}$  ( $0 \leq x \leq 1$ ), in which the broadening of the diffusion pathways should lead to enhanced transport, while the decreasing site disorder should be detrimental. The combined effect leads to only minor changes in the observed transport, showing that, in more complex materials, competing effects can be at play. Depending on the predominant diffusion pathway, these locally competing effects can even be dominating, as seen in less isotropic materials such as  $\text{Li}_{10}\text{Ge}_{1-x}\text{Sn}_x\text{P}_2\text{S}_{12}$ ,<sup>30</sup> or cancel each other out in materials with isotropic diffusion pathways such as the  $\text{Li}^+$  argyrodites.

## 5. CONCLUSION

In this work,  $\text{Se}^{2-}$  substitution within  $\text{Li}_6\text{PS}_{5-x}\text{Se}_x\text{Br}$  ( $0 \leq x \leq 1$ ) was performed to study the effect of the changing lattice polarizability, as well as the influence of the  $\text{Br}^-/\text{Ch}^{2-}$  exchange on the free chalcogen  $\text{Ch}^{2-}$ -site, on the structure and lithium transport properties. Using a combination of X-ray diffraction, neutron pair distribution function analysis, and electrochemical impedance spectroscopy, the influence of the structural changes brought on by an increasing Se content on the associated lithium transport behavior was elucidated. With increasing  $\text{Se}^{2-}$  substitution, an increase in the lattice parameters and the occupancy of the  $16e$  Wyckoff position by  $\text{Se}^{2-}$ , corresponding to the formation of  $\text{PS}_3\text{Se}^{3-}$  polyhedra, was observed. In addition, a drastic decrease in the  $\text{Br}^-/\text{Ch}^{2-}$  site disorder was also observed. These changes in the structure lead to changes in the local  $\text{Li}^+$  sublattice, inducing a rearrangement of  $\text{Li}^+$  from the  $24g$  to the  $48h$  site and a widening of the diffusion pathways.

Impedance spectroscopy and speed of sound measurements showed that, with a change in the lattice softness, both the Arrhenius prefactor and activation energy are affected. In addition, while the broadening of the  $\text{Li}^+$  diffusion pathways should be more beneficial for the ionic transport, the vanishing site disorder with Se substitution seems to counteract the effect of the  $\text{Li}^+$  sublattice. While the highest reported value for  $\text{Li}^+$  conductivity in the argyrodite structure so far of  $3.9 \text{ mS} \cdot \text{cm}$  was found, this work highlights the importance of competing structural considerations in the optimization of ionic conductivity in lithium thiophosphate superionic conductors and further emphasizes that a better understanding of dynamic lattice effects on ionic transport is still required.

## ■ ASSOCIATED CONTENT

### S Supporting Information

The Supporting Information is available free of charge on the ACS Publications website at DOI: [10.1021/acs.inorgchem.8b02443](https://doi.org/10.1021/acs.inorgchem.8b02443).

All structural tables, as obtained from the Rietveld refinements; Raman spectra; speed of sound data; and scanning electron micrographs and energy-dispersive X-ray spectrographs (PDF)

## ■ AUTHOR INFORMATION

### Corresponding Author

\*E-mail: [wolfgang.g.zeier@pc.jlug.de](mailto:wolfgang.g.zeier@pc.jlug.de).

### ORCID

Wolfgang G. Zeier: [0000-0001-7749-5089](https://orcid.org/0000-0001-7749-5089)

## Notes

The authors declare no competing financial interest.

## ACKNOWLEDGMENTS

We thank Oak Ridge National Lab for access to the NOMAD beamline (IPTS-19114) that contributed to the results presented here. The research was supported by the Deutsche Forschungsgemeinschaft (DFG) under grant number ZE 1010/4-1. S.P.C. gratefully acknowledges the Alexander von Humboldt Foundation for financial support through a Postdoctoral Fellowship. R.K. acknowledges support by the Funds of the Chemical Industry (FCI).

## REFERENCES

- (1) Janek, J.; Zeier, W. G. A Solid Future for Battery Development. *Nat. Energy* **2016**, *1*, 16141.
- (2) Bachman, J. C.; Muy, S.; Grimaud, A.; Chang, H. H.; Pour, N.; Lux, S. F.; Paschos, O.; Maglia, F.; Lupart, S.; Lamp, P.; Giordano, L.; Shao-Horn, Y. Inorganic Solid-State Electrolytes for Lithium Batteries: Mechanisms and Properties Governing Ion Conduction. *Chem. Rev.* **2016**, *116*, 140–162.
- (3) Park, K. H.; Bai, Q.; Kim, D. H.; Oh, D. Y.; Zhu, Y.; Mo, Y. Design Strategies, Practical Considerations, and New Solution Processes of Sulfide Solid Electrolytes for All-Solid-State Batteries. *Adv. Energy Mater.* **2018**, *8*, 1800035.
- (4) Hori, S.; Suzuki, K.; Hirayama, M.; Kato, Y.; Saito, T.; Yonemura, M.; Kanno, R. Synthesis, Structure, and Ionic Conductivity of Solid Solution,  $\text{Li}_{10+\delta}\text{M}_{1+\delta}\text{P}_{2-\delta}\text{S}_{12}$  ( $\text{M} = \text{Si}, \text{Sn}$ ). *Faraday Discuss.* **2014**, *176*, 83–94.
- (5) Kamaya, N.; Homma, K.; Yamakawa, Y.; Hirayama, M.; Kanno, R.; Yonemura, M.; Kamiyama, T.; Kato, Y.; Hama, S.; Kawamoto, K.; Mitsui, A. A Lithium Superionic Conductor. *Nat. Mater.* **2011**, *10*, 682–686.
- (6) Kwon, O.; Hirayama, M.; Suzuki, K.; Kato, Y.; Saito, T.; Yonemura, M.; Kamiyama, T.; Kanno, R. Synthesis, Structure, and Conduction Mechanism of the Lithium Superionic Conductor  $\text{Li}_{10+\delta}\text{Ge}_{1+\delta}\text{P}_{2-\delta}\text{S}_{12}$ . *J. Mater. Chem. A* **2015**, *3*, 438–446.
- (7) Kato, Y.; Hori, S.; Saito, T.; Suzuki, K.; Hirayama, M.; Mitsui, A.; Yonemura, M.; Iba, H.; Kanno, R. High-Power All-Solid-State Batteries Using Sulfide Superionic Conductors. *Nat. Energy* **2016**, *1*, 16030.
- (8) Mo, Y.; Ong, S. P.; Ceder, G. First Principles Study of the  $\text{Li}_{10}\text{GeP}_2\text{S}_{12}$  Lithium Super Ionic Conductor Material. *Chem. Mater.* **2012**, *24*, 15–17.
- (9) Bron, P.; Johansson, S.; Zick, K.; Schmedt auf der Günne, J.; Günne, D.; Dehnen, S. S.; Roling, B.  $\text{Li}_{10}\text{SnP}_2\text{S}_{12}$  - An Affordable Lithium Superionic Conductor. *J. Am. Chem. Soc.* **2013**, *135*, 15694–15697.
- (10) Kuhn, A.; Gerbig, O.; Zhu, C.; Falkenberg, F.; Maier, J.; Lotsch, B. V. A New Ultrafast Superionic Li-Conductor: Ion Dynamics in  $\text{Li}_{11}\text{Si}_2\text{PS}_{12}$  and Comparison with Other Tetragonal LGPS-Type Electrolytes. *Phys. Chem. Chem. Phys.* **2014**, *16*, 14669–14674.
- (11) Kuhn, A.; Duppel, V.; Lotsch, B. V. Tetragonal  $\text{Li}_{10}\text{GeP}_2\text{S}_{12}$  and  $\text{Li}_7\text{GePS}_8$  – Exploring the Li Ion Dynamics in LGPS Li Electrolytes. *Energy Environ. Sci.* **2013**, *6*, 3548–3552.
- (12) Seino, Y.; Ota, T.; Takada, K.; Hayashi, A.; Tatsumisago, M. A Sulphide Lithium Super Ion Conductor Is Superior to Liquid Ion Conductors for Use in Rechargeable Batteries. *Energy Environ. Sci.* **2014**, *7*, 627–631.
- (13) Seino, Y.; Nakagawa, M.; Senga, M.; Higuchi, H.; Takada, K.; Sasaki, T. Analysis of the Structure and Degree of Crystallisation of  $70\text{Li}_2\text{S}-30\text{P}_2\text{S}_5$  Glass Ceramic. *J. Mater. Chem. A* **2015**, *3*, 2756–2761.
- (14) Busche, M. R.; Weber, D. A.; Schneider, Y.; Dietrich, C.; Wenzel, S.; Leichtweiss, T.; Schröder, D.; Zhang, W.; Weigand, H.; Walter, D.; Sedlmaier, S. J.; Houtarde, D.; Nazar, L. F.; Janek, J. In Situ Monitoring of Fast Li-Ion Conductor  $\text{Li}_7\text{P}_3\text{S}_{11}$  Crystallization Inside a Hot-Press Setup. *Chem. Mater.* **2016**, *28*, 6152–6165.
- (15) Muramatsu, H.; Hayashi, A.; Ohtomo, T.; Hama, S.; Tatsumisago, M. Structural Change of  $\text{Li}_2\text{S}-\text{P}_2\text{S}_5$  Sulfide Solid Electrolytes in the Atmosphere. *Solid State Ionics* **2011**, *182*, 116–119.
- (16) Ohtomo, T.; Mizuno, F.; Hayashi, A.; Tadanaga, K.; Tatsumisago, M. Electrical and Electrochemical Properties of  $\text{Li}_2\text{S}-\text{P}_2\text{S}_5-\text{P}_2\text{O}_5$  Glass–Ceramic Electrolytes. *J. Power Sources* **2005**, *146*, 715–718.
- (17) Minami, K.; Hayashi, A.; Tatsumisago, M. Preparation and Characterization of Lithium Ion Conducting  $\text{Li}_2\text{S}-\text{P}_2\text{S}_5-\text{GeS}_2$  Glasses and Glass-Ceramics. *J. Non-Cryst. Solids* **2010**, *356*, 2666–2669.
- (18) Ujiie, S.; Hayashi, A.; Tatsumisago, M. Structure, Ionic Conductivity and Electrochemical Stability of  $\text{Li}_2\text{S}-\text{P}_2\text{S}_5-\text{LiI}$  Glass and Glass–Ceramic Electrolytes. *Solid State Ionics* **2012**, *211*, 42–45.
- (19) Dietrich, C.; Weber, D. A.; Sedlmaier, S. J.; Indris, S.; Culver, S. P.; Walter, D.; Zeier, W. G. Lithium Ion Conductivity in  $\text{Li}_2\text{S}-\text{P}_2\text{S}_5$  Glasses. *J. Mater. Chem. A* **2017**, *5*, 18111–18119.
- (20) Kraft, M. A.; Culver, S. P.; Calderon, M.; Böcher, F.; Krauskopf, T.; Senyshyn, A.; Dietrich, C.; Zevalkink, A.; Janek, J.; Zeier, W. G. Influence of Lattice Polarizability on the Ionic Conductivity in the Lithium Superionic Argyrodites  $\text{Li}_6\text{PS}_5\text{X}$  ( $\text{X} = \text{Cl}, \text{Br}, \text{I}$ ). *J. Am. Chem. Soc.* **2017**, *139*, 10909–10918.
- (21) Minafra, N.; Culver, S. P.; Krauskopf, T.; Senyshyn, A.; Zeier, W. G. Effect of Si Substitution on the Structural and Transport Properties of Superionic Li-Arnyrodites. *J. Mater. Chem. A* **2018**, *6*, 645–651.
- (22) Deiseroth, H. J.; Kong, S. T.; Eckert, H.; Vannahme, J.; Reiner, C.; Zaif, T.; Schlosser, M.  $\text{Li}_6\text{PS}_5\text{X}$ : A Class of Crystalline Li-Rich Solids with an Unusually High  $\text{Li}^+$  Mobility. *Angew. Chem., Int. Ed.* **2008**, *47*, 755–758.
- (23) Rayavarapu, P. R.; Sharma, N.; Peterson, V. K.; Adams, S. Variation in Structure and  $\text{Li}^+$ -Ion Migration in Argyrodite-Type  $\text{Li}_6\text{PS}_5\text{X}$  ( $\text{X} = \text{Cl}, \text{Br}, \text{I}$ ) Solid Electrolytes. *J. Solid State Electrochem.* **2012**, *16*, 1807–1813.
- (24) Wang, Z.; Shao, G. Theoretical Design of Solid Electrolytes with Superb Ionic Conductivity: Alloying Effect on  $\text{Li}^+$  Transportation in Cubic  $\text{Li}_6\text{PA}_5\text{X}$  Chalcogenides. *J. Mater. Chem. A* **2017**, *5*, 21846–21857.
- (25) Holzmann, T.; Schoop, L. M.; Ali, M. N.; Moudrakovski, I.; Gregori, G.; Maier, J.; Cava, R. J.; Lotsch, B. V.  $\text{Li}_{0.6}[\text{Li}_{0.2}\text{Sn}_{0.8}\text{S}_2]$  – a Layered Lithium Superionic Conductor. *Energy Environ. Sci.* **2016**, *9*, 2578–2585.
- (26) de Klerk, N. J. J.; Rosloń, I.; Wagemaker, M. Diffusion Mechanism of Li Argyrodite Solid Electrolytes for Li-Ion Batteries and Prediction of Optimized Halogen Doping: The Effect of Li Vacancies, Halogens, and Halogen Disorder. *Chem. Mater.* **2016**, *28*, 7955–7963.
- (27) Coelho, A. A. *TOPAS-Academic*; Brisbane, Australia, 2007.
- (28) Farrow, C. L.; Juhas, P.; Liu, J. W.; Bryndin, D.; Božin, E. S.; Bloch, J.; Proffen, T.; Billinge, S. J. L. PDFfit2 and PDFgui: Computer Programs for Studying Nanostructure in Crystals. *J. Phys.: Condens. Matter* **2007**, *19*, 335219.
- (29) Weber, D. A.; Senyshyn, A.; Weldert, K. S.; Wenzel, S.; Zhang, W.; Kaiser, R.; Berendts, S.; Janek, J.; Zeier, W. G. Structural Insights and 3D Diffusion Pathways within the Lithium Superionic Conductor  $\text{Li}_{10}\text{GeP}_2\text{S}_{12}$ . *Chem. Mater.* **2016**, *28*, 5905–5915.
- (30) Krauskopf, T.; Culver, S. P.; Zeier, W. G. Bottleneck of Diffusion and Inductive Effects in  $\text{Li}_{10}\text{Ge}_{1-x}\text{Sn}_x\text{P}_2\text{S}_{12}$ . *Chem. Mater.* **2018**, *30*, 1791–1798.
- (31) Krauskopf, T.; Pompe, C.; Kraft, M.; Zeier, W. G. Influence of Lattice Dynamics on  $\text{Na}^+$ -Transport in the Solid Electrolyte  $\text{Na}_3\text{PS}_{4-x}\text{Se}_x$ . *Chem. Mater.* **2017**, *29*, 8859–8869.
- (32) May, A. F.; Snyder, G. J. Introduction to Modeling Thermoelectric Transport at High Temperatures. In *Thermoelectrics Handbook: Thermoelectrics and its Energy Harvesting*; Rowe, D. M., Ed.; CRC Press: Boca Raton, FL, 2012.

- (33) Anderson, O. L. A Simplified Method for Calculating the Debye Temperature from Elastic Constants. *J. Phys. Chem. Solids* **1963**, *24*, 909–917.
- (34) He, X.; Zhu, Y.; Mo, Y. Conductors. *Nat. Commun.* **2017**, *8*, 15893.
- (35) Shannon, R. D. Revised Effective Ionic Radii and Systematic Studies of Interatomic Distances in Halides and Chalcogenides Acta. *Acta Crystallogr., Sect. A: Cryst. Phys., Diff., Theor. Gen. Crystallogr.* **1976**, *32*, 751–767.
- (36) Zeier, W. G.; Zhou, S.; Lopez-Bermudez, B.; Page, K.; Melot, B. C. Dependence of the Li-Ion Conductivity and Activation Energies on the Crystal Structure and Ionic Radii in  $\text{Li}_6\text{MLa}_2\text{Ta}_2\text{O}_{12}$ . *ACS Appl. Mater. Interfaces* **2014**, *6*, 10900–10907.
- (37) Irvine, J. T. S.; Sinclair, D. C.; West, A. R. Electroceramics: Characterization by Impedance Spectroscopy. *Adv. Mater.* **1990**, *2*, 132–138.
- (38) Brug, G. J.; van den Eeden, A. L. G.; Sluyters-Rehbach, M.; Sluyters, J. H. The Analysis of Electrode Impedances Complicated by the Presence of a Constant Phase Element. *J. Electroanal. Chem. Interfacial Electrochem.* **1984**, *176*, 275–295.
- (39) Zhang, L.; Yang, K.; Mi, J.; Lu, L.; Zhao, L.; Wang, L.; Li, Y.; Zeng, H.  $\text{Na}_3\text{PSe}_4$ : A Novel Chalcogenide Solid Electrolyte with High Ionic Conductivity. *Adv. Energy Mater.* **2015**, *5*, 1501294.
- (40) Bo, S.-H.; Wang, Y.; Ceder, G. Structural and Na-Ion Conduction Characteristics of  $\text{Na}_3\text{PS}_x\text{Se}_{4-x}$ . *J. Mater. Chem. A* **2016**, *4*, 9044–9053.
- (41) Krauskopf, T.; Muy, S.; Culver, S. P.; Ohno, S.; Delaire, O.; Shao-Horn, Y.; Zeier, W. G. Comparing the Descriptors for Investigating the Influence of Lattice Dynamics on Ionic Transport Using the Superionic Conductor  $\text{Na}_3\text{PS}_{4+x}\text{Se}_x$ . *J. Am. Chem. Soc.* **2018**, DOI: [10.1021/jacs.8b09340](https://doi.org/10.1021/jacs.8b09340).
- (42) Culver, S. P.; Krauskopf, T.; Koerver, R.; Zeier, W. G. Designing Ionic Conductors: The Interplay between Structural Phenomena and Interfaces in Thiophosphatebased Solid-State Batteries. *Chem. Mater.* **2018**, *30*, 4179–4192.
- (43) Rice, M. J.; Roth, W. L. Ionic Transport in Superionic Conductors: A Theoretical Model. *J. Solid State Chem.* **1972**, *4*, 294–310.
- (44) Vineyard, G. H. Frequency Factors and Isotope Effects in Solid State Rate Processes. *J. Phys. Chem. Solids* **1957**, *3*, 121–127.
- (45) Meyer, W.; Neldel, H. Über Die Beziehungen Zwischen Der Energiekonstanten Und Der Mengenkonstanten a in Der Leitwerts Temperaturformel Bei Oxydischen Halbleitern. *Z. Technol. Phys.* **1937**, 588.
- (46) Muy, S.; Bachmann, J. C.; Chang, H.-H.; Giordano, L.; Maglia, F.; Lupart, S.; Lamp, P.; Zeier, W. G.; Shao. The Role of Lattice Dynamics on the Lithium Conductivity of  $\text{Li}_3\text{PO}_4\text{-Li}_3\text{VO}_4\text{-Li}_4\text{GeO}_4$  Lithium Superionic Conductors. *Chem. Mater.* **2018**, *30*, 5573–5582.
- (47) Yelon, A.; Movaghari, B.; Crandall, R. S. Multi-Excitation Entropy: Its Role in Thermodynamics and Kinetics. *Rep. Prog. Phys.* **2006**, *69*, 1145–1194.
- (48) Yelon, A.; Movaghari, B.; Branz, H. M. Origin and Consequences of the Compensation (Meyer-Neldel) Law. *Phys. Rev. B: Condens. Matter Mater. Phys.* **1992**, *46*, 12244–12250.
- (49) Muy, S.; Bachman, J. C.; Giordano, L.; Chang, H.-H.; Abernathy, D. L.; Bansal, D.; Delaire, O.; Hori, S.; Kanno, R.; Maglia, F.; Lupart, S.; Lamp, P.; Shao-Horn, Y. Tuning Mobility and Stability of Lithium Ion Conductors Based on Lattice Dynamics. *Energy Environ. Sci.* **2018**, *11*, 850–859.
- (50) Wang, Y.; Richards, W. D.; Ong, S. P.; Miara, L. J.; Kim, J. C.; Mo, Y.; Ceder, G. Design Principles for Solid-State Lithium Superionic Conductors. *Nat. Mater.* **2015**, *14*, 1026–1031.
- (51) Guin, M.; Tietz, F. Survey of the Transport Properties of Sodium Superionic Conductor Materials for Use in Sodium Batteries. *J. Power Sources* **2015**, *273*, 1056–1064.
- (52) Zeier, W. G. Structural Limitations for Optimizing Garnet-Type Solid Electrolytes: A Perspective. *Dalt. Trans.* **2014**, *43*, 16133–16138.